Supporting Information:

Colossal zero-field cooled exchange bias via tuning compensated ferrimagnetic in kagome metals

Haowei Zhou,[1] Yili Cao,[1,*] Sergii Khmelevskyi,[2] Qinghua Zhang,[3] Shixin Hu,[4] Maxim Avdeev,[5,6] Chin-Wei Wang,[7] Rui Zhou,[3] Chengyi Yu,[1] Xin Chen,[1] Qiheng Li,[1] Jun Miao,[1] Qiang Li,[1] Kun Lin[1] and Xianran Xing[1,*]

[1]Beijing Advanced Innovation Center for Materials Genome Engineering, Institute of Solid State Chemistry, University of Science and Technology Beijing, Beijing, 100083, China

[2]Vienna Scientific Cluster Research Center, Technical University of Vienna, Operngasse 10, Vienna A-1040, Austria

[3]Institute of Physics, Chinese Academy of Sciences, Beijing 100190, China.

[4]Institute of Applied Magnetics, Key Laboratory for Magnetism and Magnetic Materials of the Ministry of Education, Lanzhou University, Lanzhou 730000, China

[5]Australian Nuclear Science and Technology Organisation, Lucas Heights, New South Wales 2234, Australia

[6]School of Chemistry, The University of Sydney, Sydney, New South Wales 2006, Australia

[7]Neutron Group, National Synchrotron Radiation Research Center, Hsinchu 30076, Taiwan

*Corresponding authors.yilicao@ustb.edu.cn (Y.L.C.); xing@ustb.edu.cn (X.R.X.)

Materials and Methods.

Figures and Tables.

References.

Materials and Methods.

Sample preparation.

A high-purity (99.99%) metal raw material with precisely calculated molar ratios was prepared for all $Ho_2Fe_{17}Mn_\delta$ series samples (δ = 0, 1, 3, 4, 4.5, 4.75, 5, 5.5, 6, 7; denoted as **Mn0**, **Mn1**, **Mn3**, **Mn4**, **Mn4.5**, **Mn4.75**, **Mn5**, **Mn5.5**, **Mn6** and **Mn7**, respectively). The ingots were melted and turned over more than four times under a high-purity argon atmosphere. To obtain the target sample, the samples are wrapped in molybdenum foil and sealed in a quartz tube, followed by a heat treatment at 1473 K for three days, and then quenched with ice water. The ingots were ground into fine powder for synchrotron radiation X-ray diffraction (SXRD), neutron powder diffraction (NPD), magnetization measurements, Mössbauer spectrum test, and ICP-OES experiment samples.

Composition Characterization.

The real chemical composition of the target alloys was measured by Inductively Coupled Plasma-Optical Emission Spectroscopy (ICP-OES, Agilent ICPOES730, USA).

Structural Characterization.

Powder X-ray diffraction (XRD) was performed by the Lab. X-ray diffractometer (SmartLab 9 kw, Rigaku Corporation) with Cu Kα radiation. Synchrotron X-ray diffraction (SXRD) experiments were measured on the BL44B2 beamline (λ =0.7 Å) at Spring 8. The Australian Nuclear Science and Technology Organization (ANSTO) conducted temperature-dependent neutron powder diffraction (NPD) at a high-intensity neutron diffractometer (WOMBAT) with a wavelength of 2.41 Å. The software FULLPROF was used to carry out the full-profile Rietveld refinements of the SXRD and NPD patterns. The high-angle annular dark-field (HAADF), the annular bright field (ABF) and the Electron Energy Loss Spectroscopy (EELS) patterns were measured on an aberration-corrected TEI Tecnai ETEM, JEM-ARM 200F. All the images are

processed by Gatan Digital Micrograph software.

Magnetization measurements.

Physics property measuring system (PPMS, Quantum Design) was used to quantify temperature-dependent magnetization and magnetic field-dependent magnetization down to 1.9 K. The Superconducting Quantum Interference Device (SQUID) vibrating sample magnetometer (VSM) with an amplitude of 5 Oe was used to conduct the susceptibility experiment. Both oscillatory and high temperature ($T > T_C$) demagnetization were applied to every curve.

Mössbauer and Nuclear Magnetic Resonance spectrum measurements

The Mössbauer absorption spectra were obtained on a constant acceleration spectrometer that utilized a rhodium matrix cobalt-57 source. It was calibrated using α-Fe foil, and the isomer values were referred to α-Fe. The ^{55}Mn Nuclear Magnetic Resonance spectra at different temperature were obtained by the fast Fourier transformation of the spin-echo at zero magnetic field.

Thermal expansion of the alloy.

The linear thermal expansion curves ($\Delta L/L_0$) were measured on a thermal expansion meter (NETZSCH DIL402) along the c axis and lattice thermal expansion was determined by NPD refinement results.

Theoretic calculations.

To explore the microscopic mechanism of this phenomena we calculate the energies of different magnetic configurations in Mn5 and Mn7 2:17 alloys and inter-atomic exchange interactions between Ho, Fe and Mn magnetic sites on the first-principle basis. To this end we use Green Function Korringa-Kohn-Rostoker (KKR) band structure formalism and Local Spin Density *Approximation.*[1] The atomic disorder of Fe and Mn atoms on 12j and 4f sub-lattices was taken into account using the Coherent Potential

Approximation (CPA) technique.[2] The Ho 4f-states have been treated in the open-core scheme, similarly to our previous investigation of the exchange interactions in the pure Gd and RE-based intermetallics[3,4] (for details and discussion of the validity of this scheme see respective publications). We use Atomic Sphere Approximation (ASA) with partial wave expansion in KKR-ASA calculations up to $l_{max} = 2$. The experimental lattice constants and crystal geometry have been used.

Table S1. Composition of the $Ho_2Fe_{17}Mn_\delta$ alloy determined by inductively coupled plasma-optical emission spectroscopy (ICP-OES). Because of the volatility of Mn, the real component deviates from the nominal component.

ICP-OES	Ho (wt%)	Fe (wt%)	Mn (wt%)
$Ho_2Fe_{17}Mn_1$	25.4655	70.9395	1.3823
$Ho_2Fe_{17}Mn_3$	24.1989	67.4896	6.7423
$Ho_2Fe_{17}Mn_5$	22.2586	64.1668	11.6075
$Ho_2Fe_{17}Mn_7$	21.5000	62.1006	15.6472

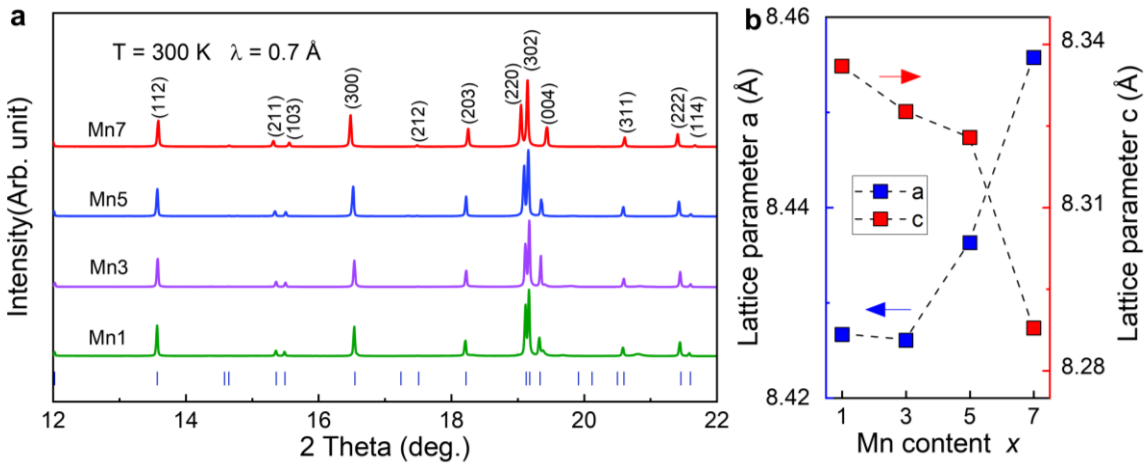

Figure S1. (a) Synchrotron X-ray powder diffraction (SXRD) patterns at room temperature for the four investigated samples: **Mn1**, **Mn3**, **Mn5** and **Mn7** ($\lambda = 0.7$ Å) annealed at 1473 K for 3 days, all samples are hexagonal phase. (b) Lattice parameters with the content of Mn. Lattice parameter *a* increases and *c* decreases continuously, evidencing Mn atoms doping into the hexagonal phase.

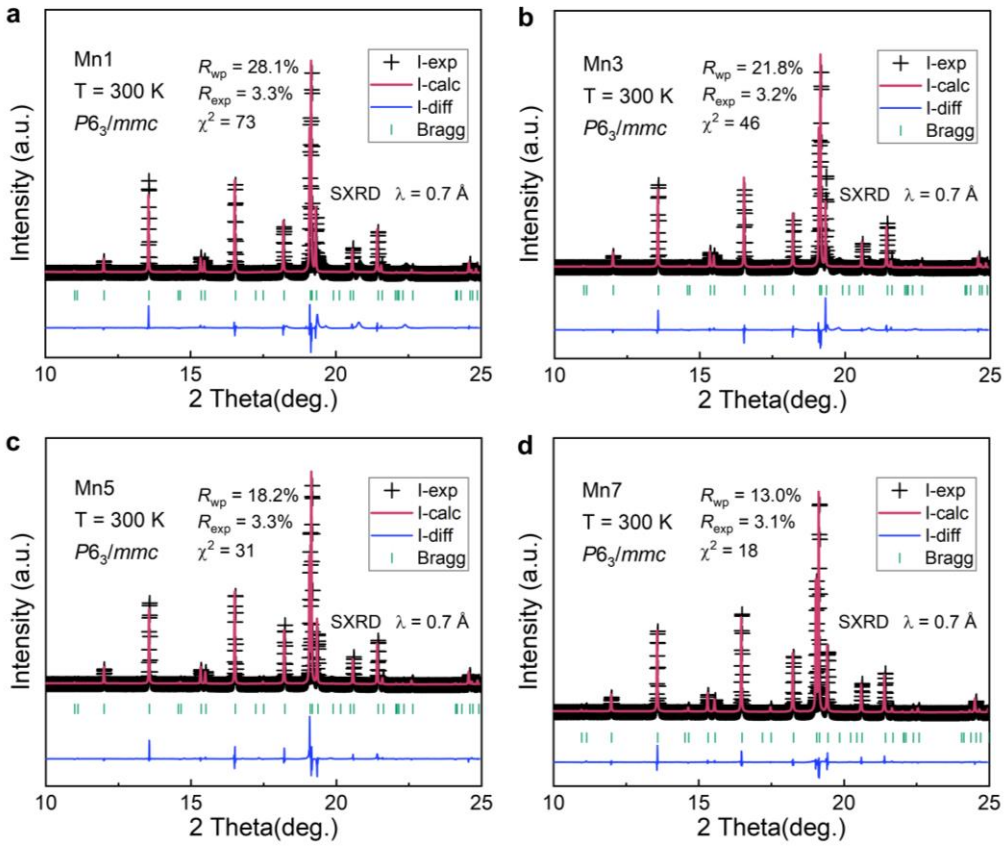

Figure S2. Rietveld refinements of synchrotron X-ray diffraction patterns for **Mn1** (a), **Mn3** (b), **Mn5** (c) and **Mn7** (d) at room temperature.

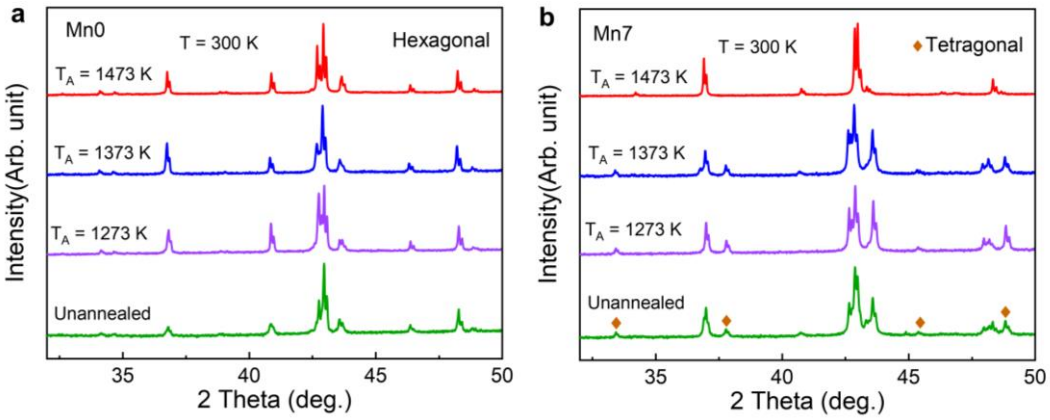

Figure S3. Room-temperature X-ray diffraction patterns for **Mn0** (a) and **Mn7** (b) under Cu Kα radiation with unannealed and various annealing temperature (denoted as T_A) at 1273 K, 1373 K and 1473 K, respectively. The tetragonal phases are shown by the brown-marked peaks in (b). The composition with high Mn doping maintains the hexagonal phase as the annealing temperature increases.

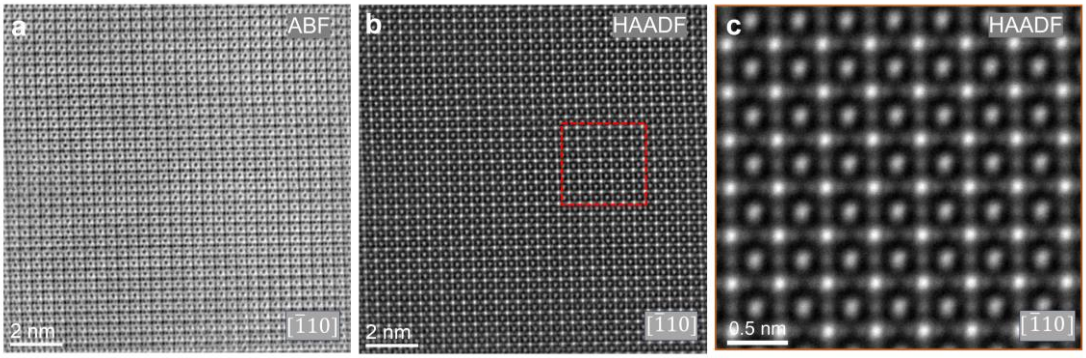

Figure S4. The ABF (a) and HAADF-STEM (b) image of **Mn5** as viewed along the [$\bar{1}$10] zone axis. (c) Enlarged random domain of the red dashed line area showing atomic planes.

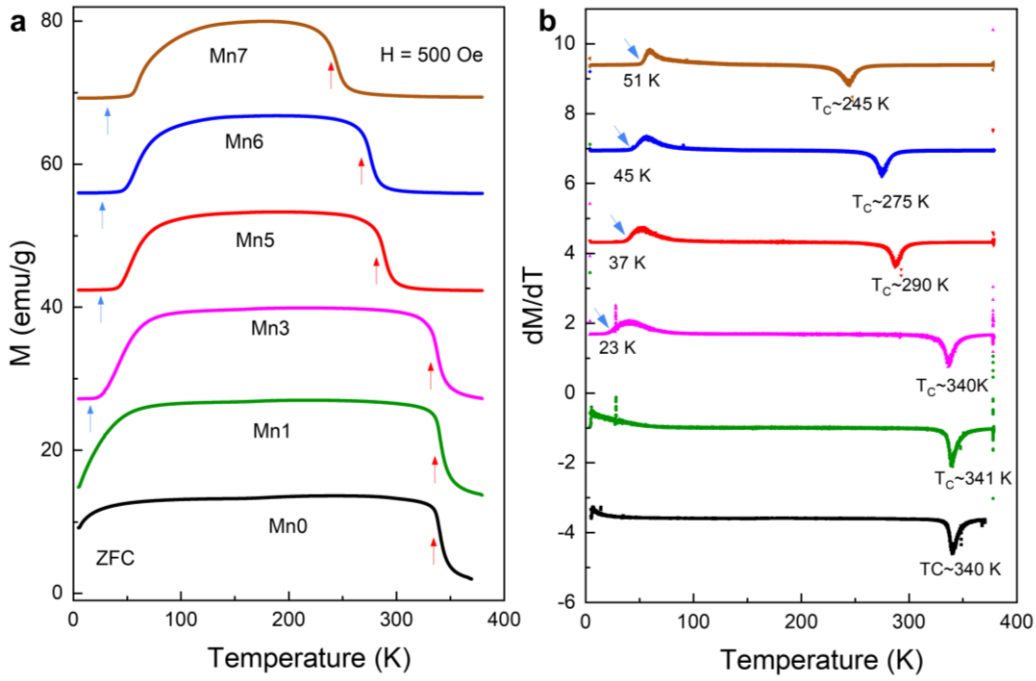

Figure S5. Temperature dependence of magnetization (a) and the differential curves (b) of **Mn0**, **Mn1**, **Mn3**, **Mn5**, **Mn6** and **Mn7** under zero field cooled (ZFC) conditions.

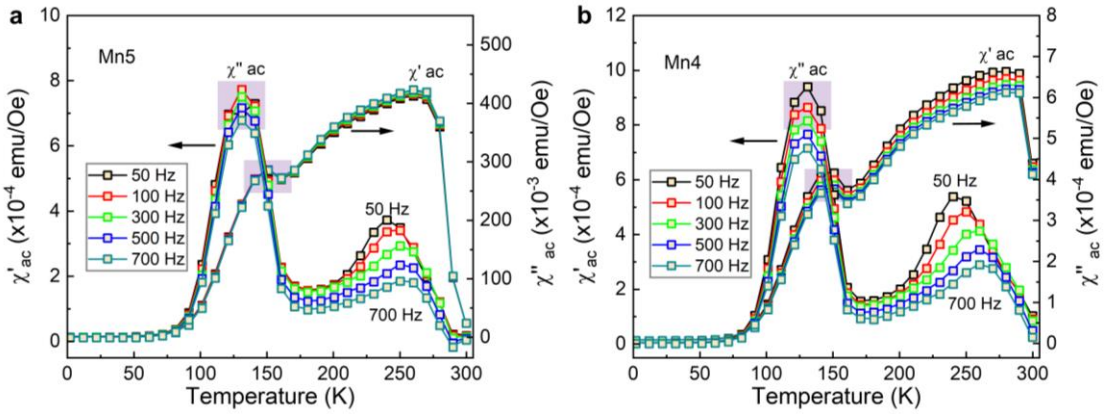

Figure S6. Real (χ') and imaginary (χ") parts of the ac susceptibility with different frequencies and an amplitude of 5Oe from 2 K to 300 K of **Mn5** (a) and **Mn4** (b).

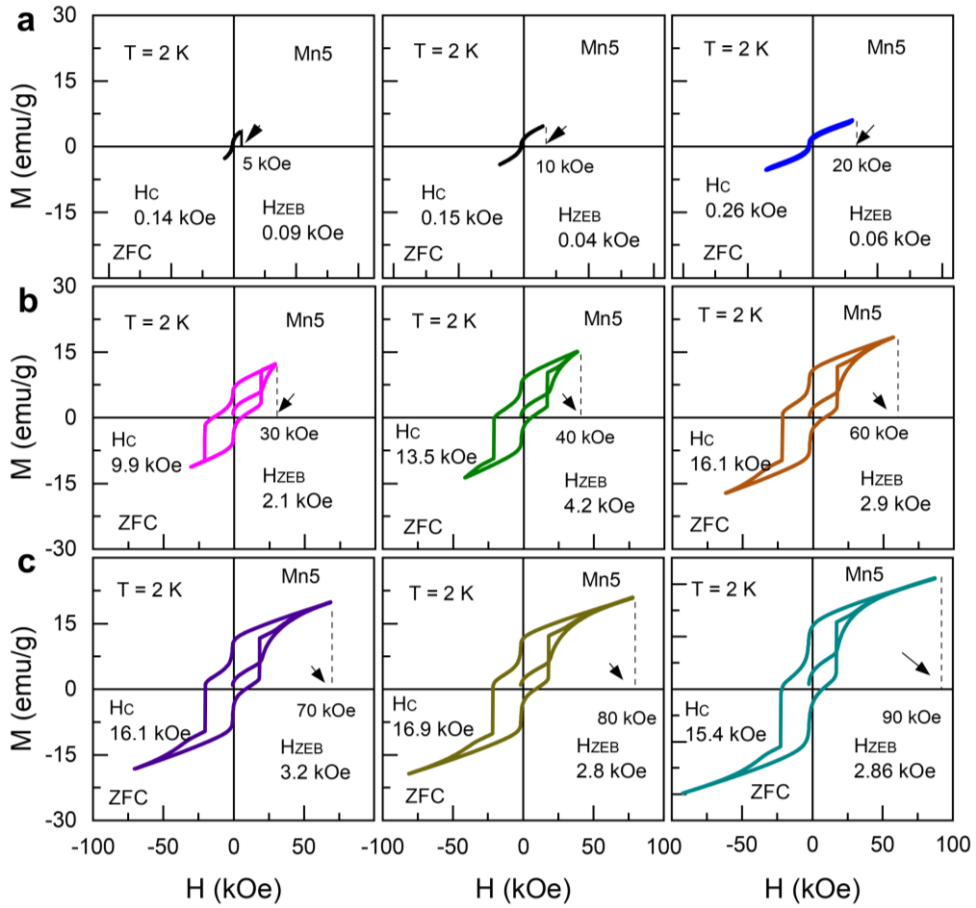

Figure S7. Magnetic hysteresis loop of **Mn5** under ZFC measured at 2 K with max magnetic field |Hmax| (a) 5 kOe, 10kOe and 20 kOe, (b) 30 kOe, 40 kOe and 60 kOe, (**c**) 70 kOe, 80 kOe and 90 kOe.

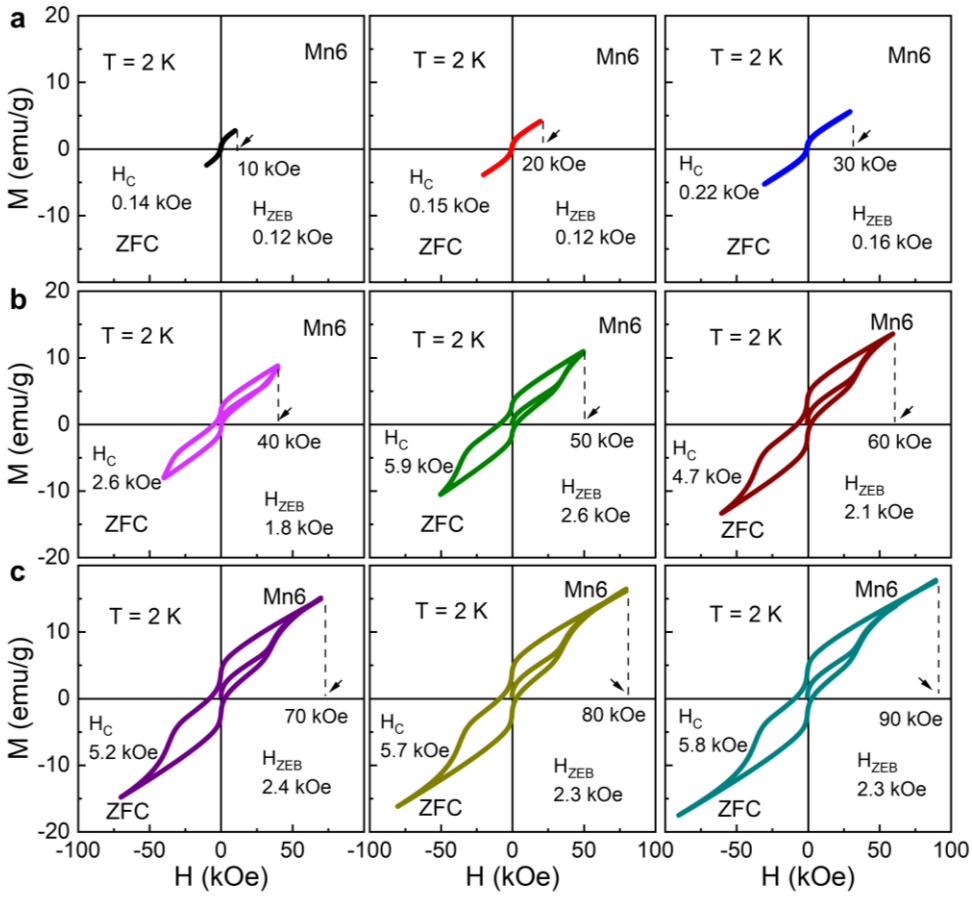

Figure S8. Magnetic hysteresis loop of **Mn6** under ZFC measured at 2 K with max magnetic field |Hmax| (a) 10 kOe, 20 kOe and 30 kOe, (b) 40 kOe, 50 kOe and 60 kOe, (**c**) 70 kOe, 80 kOe and 90 kOe.

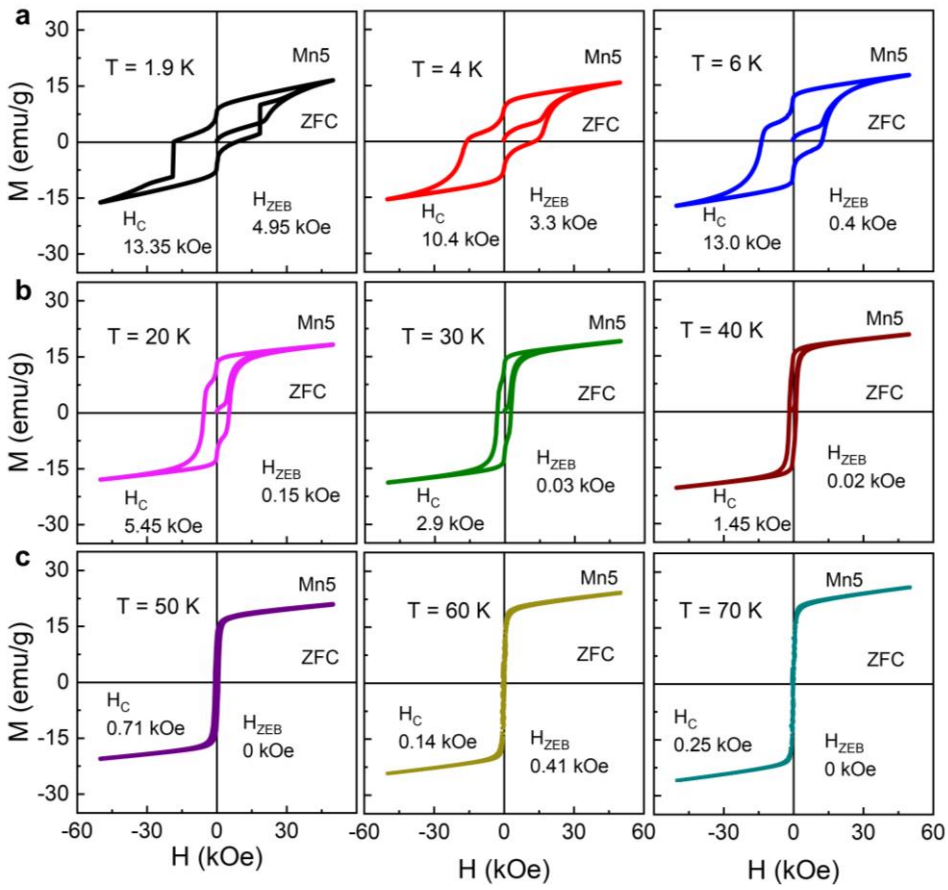

Figure S9. Magnetic hysteresis loops of **Mn5** under ZFC were measured at (a) 1.9 K, 4 K and 6 K, (b) 20 K, 30 K and 40 K, (c) 50 K, 60 K and 70 K with max magnetic field of |Hmax| = 50 kOe.

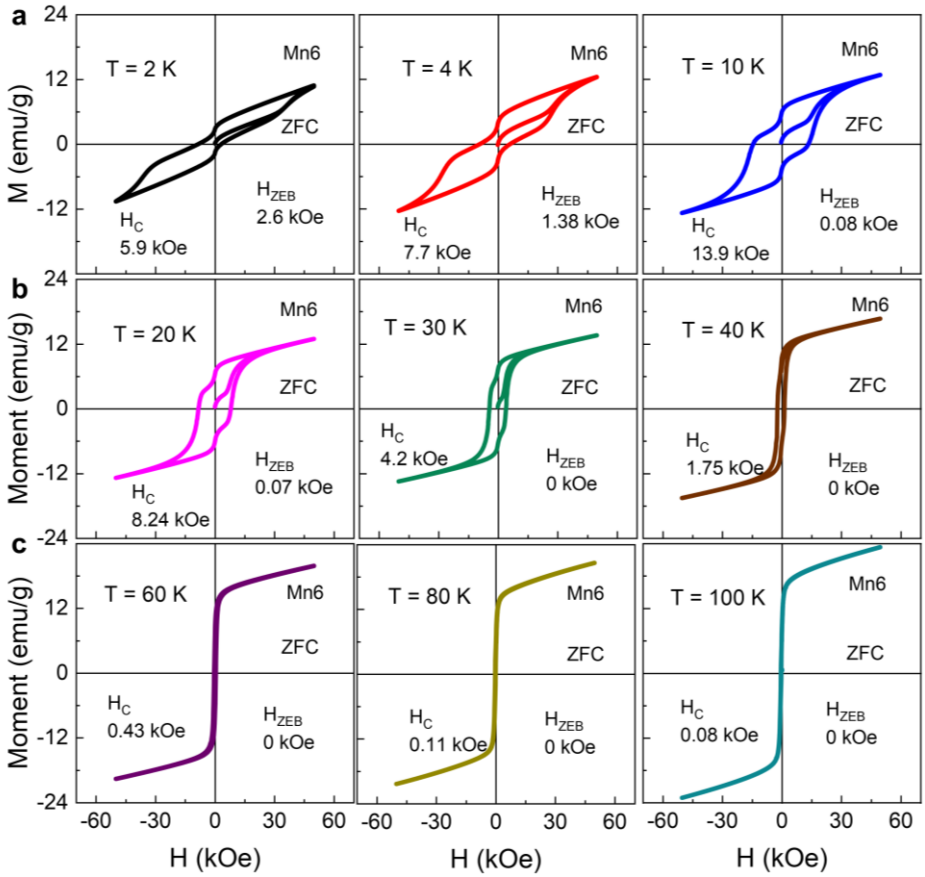

Figure S10. Magnetic hysteresis loops of **Mn6** under ZFC were measured at (a) 2 K, 4 K and 10 K, (b) 20 K, 30 K and 40 K, (c) 60 K, 80 K and 100 K with max magnetic field |Hmax| = 50 kOe.

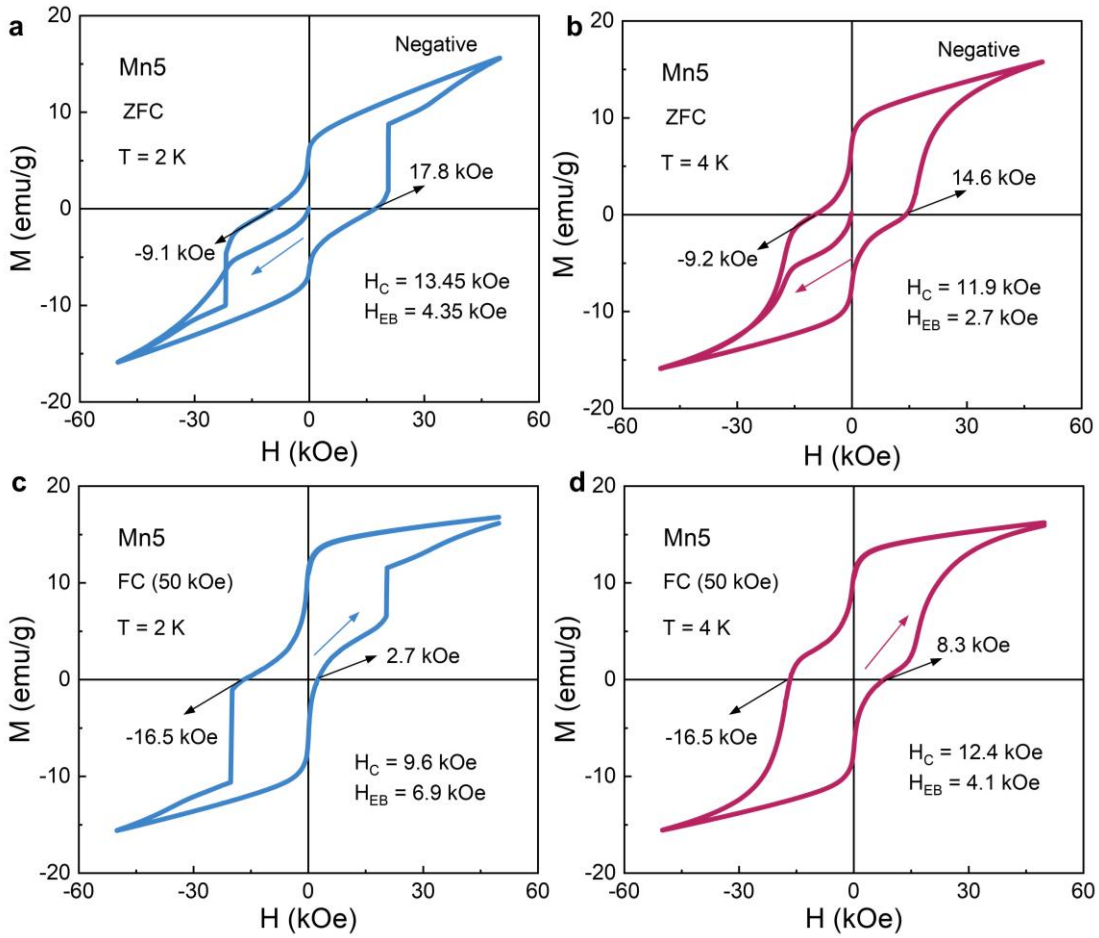

Figure S11. Magnetic hysteresis loop of **Mn5** measured of negative type (performed as 0 → -50 → 50→ -50 kOe) under ZFC condition at (a) 2 K and (b) 4 K. Magnetic hysteresis loop of Mn5 under FC (50 kOe) at 2 K (c) and (d) 4 K.

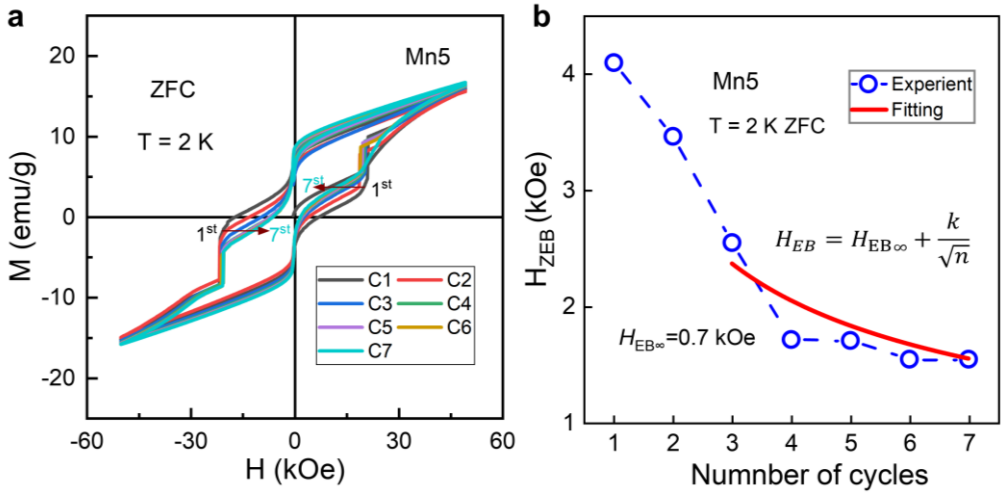

Figure S12. (a) The consecutive hysteresis loops of **Mn5** at 2 K with |Hmax| = 50 kOe measured showing the training effect, (b) it shows the number of field cycles (n), the dependence of H_{ZEB}, and $H_{EB\infty}$ is the exchange-bias field in the limit of infinite loops, the solid lines show the fit for n ⩾3, the fitting result $H_{EB\infty}$ = 0.7 kOe.

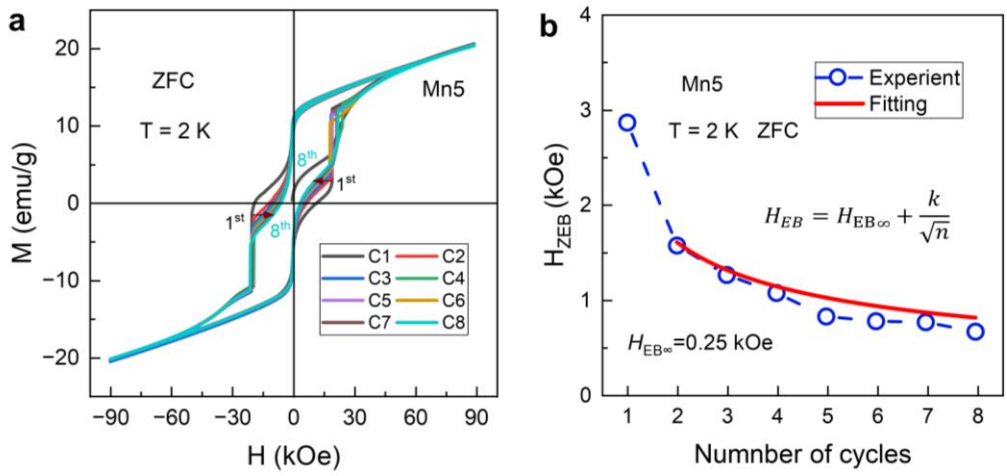

Figure S13. (a) The consecutive hysteresis loops of **Mn5** at 2 K with |Hmax| = 90 kOe measured showing the training effect, (b) it shows the number of field cycles (n), the dependence of H_{ZEB}, the solid lines show the fit for n ⩾ 2, the fitting result $H_{EB\infty}$ = 0.25 kOe.

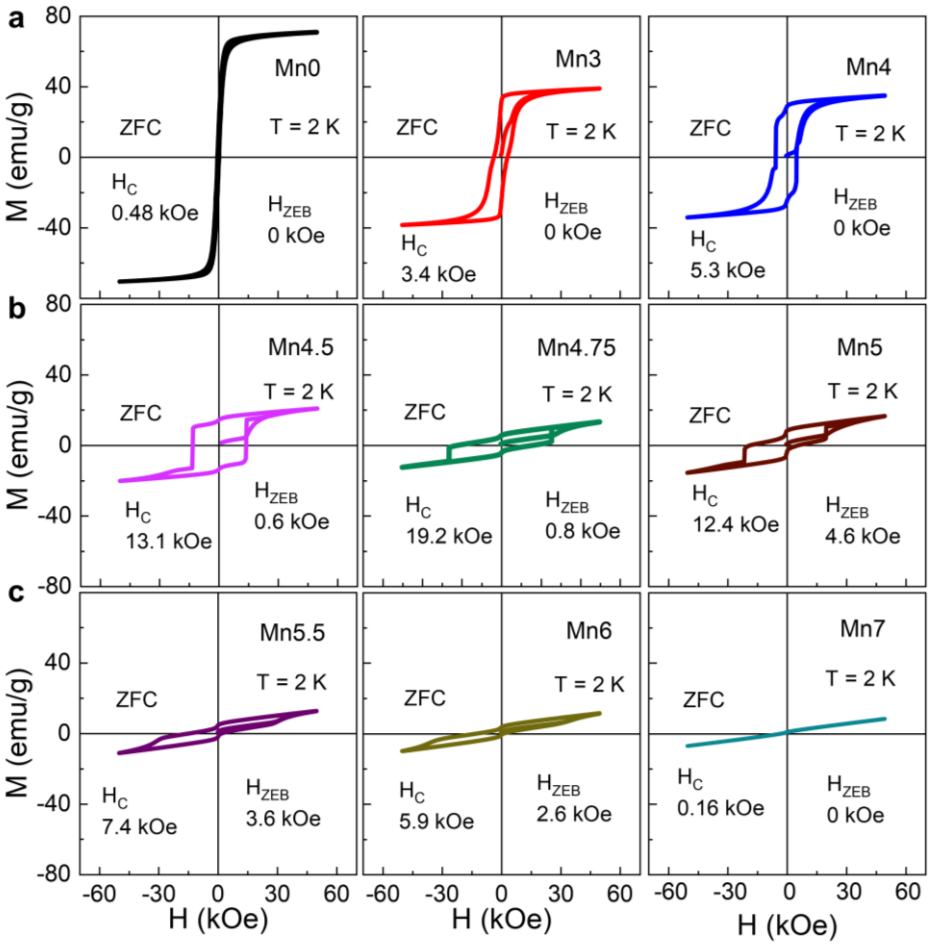

Figure S14. Magnetic hysteresis loops under ZFC were measured at 2 K with |Hmax| = 50 kOe for (a) **Mn0**, **Mn3** and **Mn4** (b) **Mn4.5**, **Mn4.75** and **Mn5,** (c) **Mn5.5**, **Mn6** and **Mn7**.

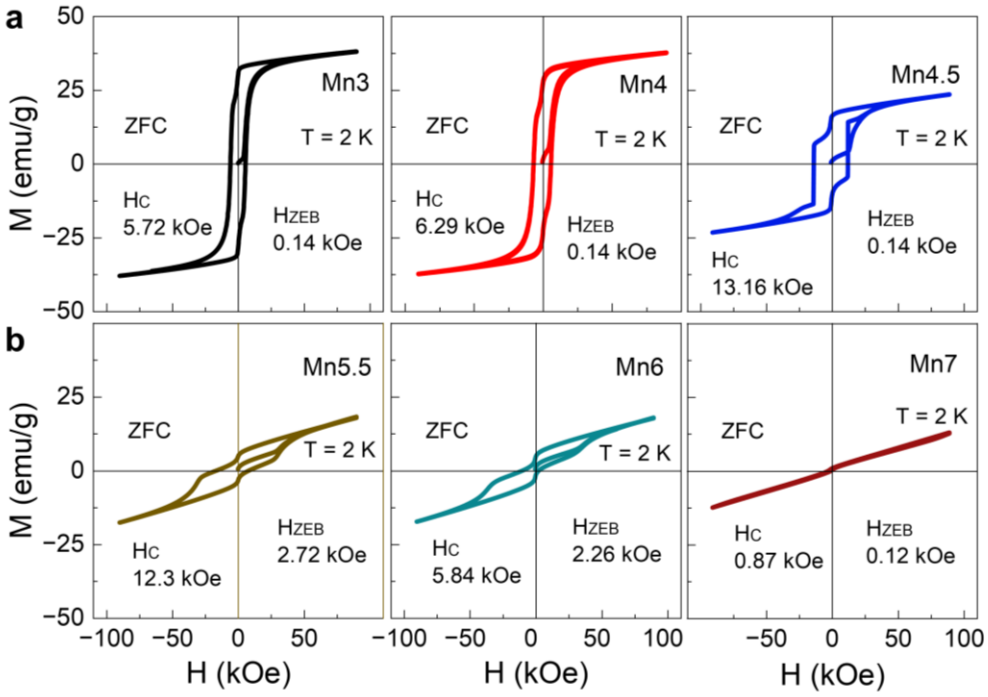

Figure S15. Magnetic hysteresis loops under ZFC were measured at 2 K with |Hmax| = 90 kOe for (a) **Mn3**, **Mn4** and **Mn4.5** (b) **Mn5.5**, **Mn6** and **Mn7**.

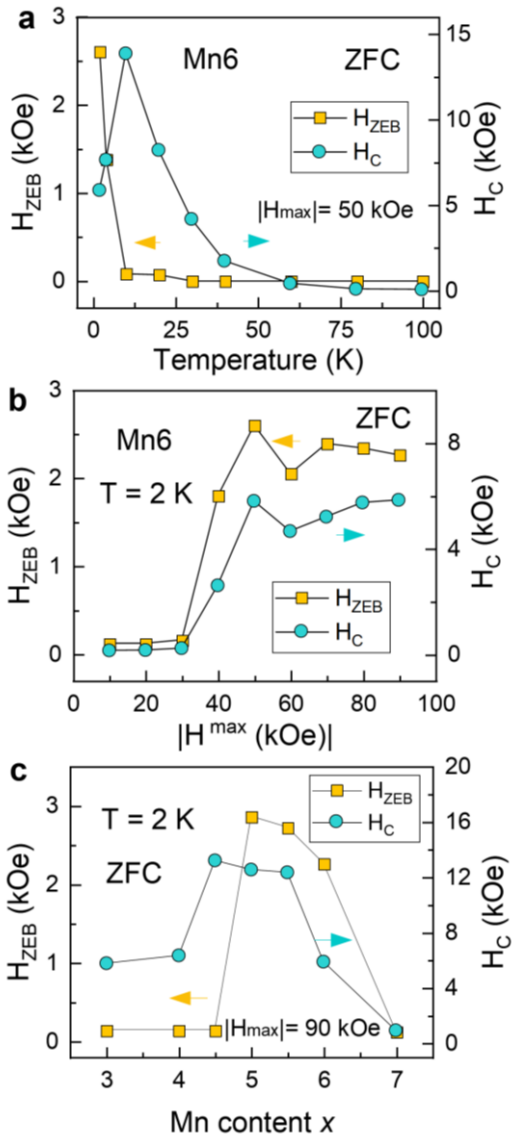

Figure S16. (a) Temperature dependence of the ZEB field (H_{ZEB}) and coercive field (H_C) for **Mn6**. (b) Magnetic field dependence of the H_{ZEB} and H_C at 2 K for **Mn6**. (c) H_{ZEB} and H_C as a function of the Mn content at 2 K with |Hmax| = 90 kOe.

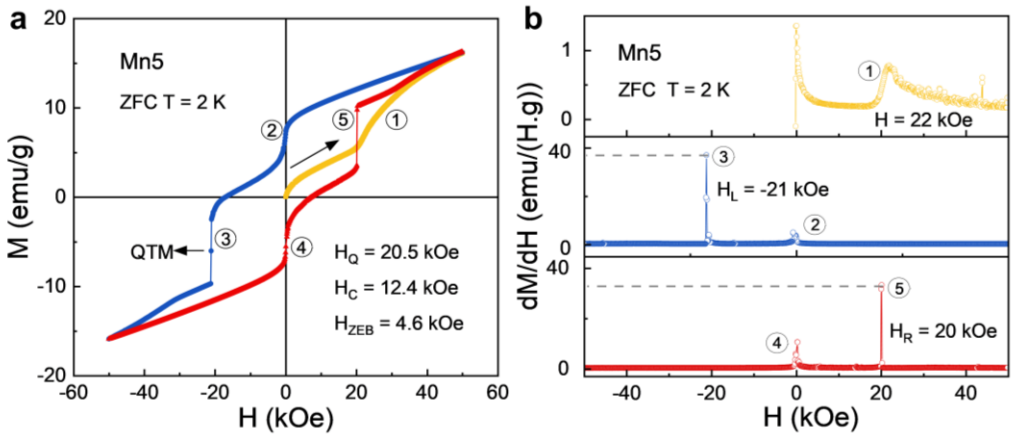

Figure S17. (a) Magnetic hysteresis loop of **Mn5** under ZFC measured at 2 K and (b) the differential curves. The hysteresis loop occurs metamagnetic transition at the virgin magnetization curve, when the magnetic field increases, the curve shows a dramatic drop in the hysteresis loop known as quantum tunneling of magnetization (QTM). This is a type of quantum activity at the macro level that is comparable to the behavior of a single-molecule magnet.[5]

Table S2. The zero-field cooling exchange bias field (H_{ZEB}) and coercive field (H_C) for typical metal materials.

ZEB materials	H_{ZEB} (kOe)	H_C (kOe)	Reference
Mn5	4.95	13.35	This work
Mn5.5	3.62	7.41	This work
Mn6	2.61	5.92	This work
$PdNCr_3$	0.35	1.35	6
$sMn_{50}Ni_{40}Sn_7Ti_3$	0.5	2.60	7
$Ga_{0.94}NMn_{3.06}$	0.51	2.50	8
$Ni_2Mn_{1.4}Ga_{0.6}$	0.86	1.00	9
$Mn_{63}Bi_{37}$	1.20	6.00	10
$Ni_{50}Mn_{37}In_{13}$	1.30	1.65	11
$Mn_{50}Ni_{40}Sn_6Si_4$	1.30	2.20	12
Mn_2PtGa	1.70	1.85	13
$Ni_{50}Mn_{34}In_{13}Fe_3$	1.70	0.88	14
$Ni_{50}Mn_{40}Sn_{10}$	2.23	1.70	15
$Mn_{3.5}Co_{0.5}N$	2.80	1.60	16
$Ni_{50}Mn_{38}Ga_{10}Sb_2$	2.93	2.10	17
$Ni_{50}Mn_{36}Co_4Sn_{10}$	2.96	2.50	18

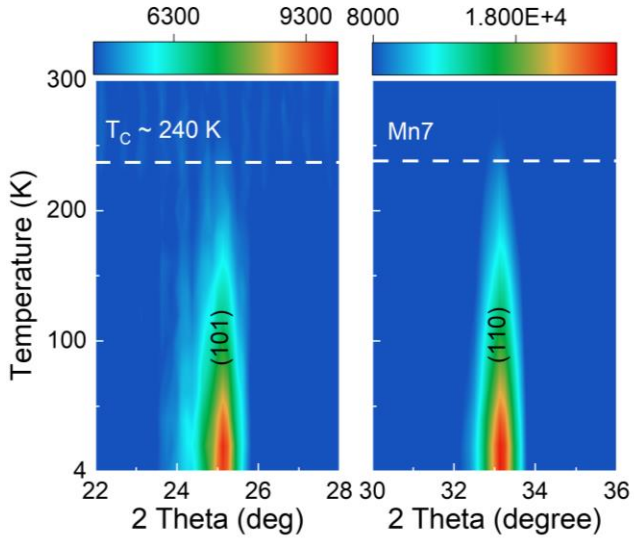

Figure S18. The contour plot of NPD intensity of (101) and (110) peaks of **Mn7** with different temperature.

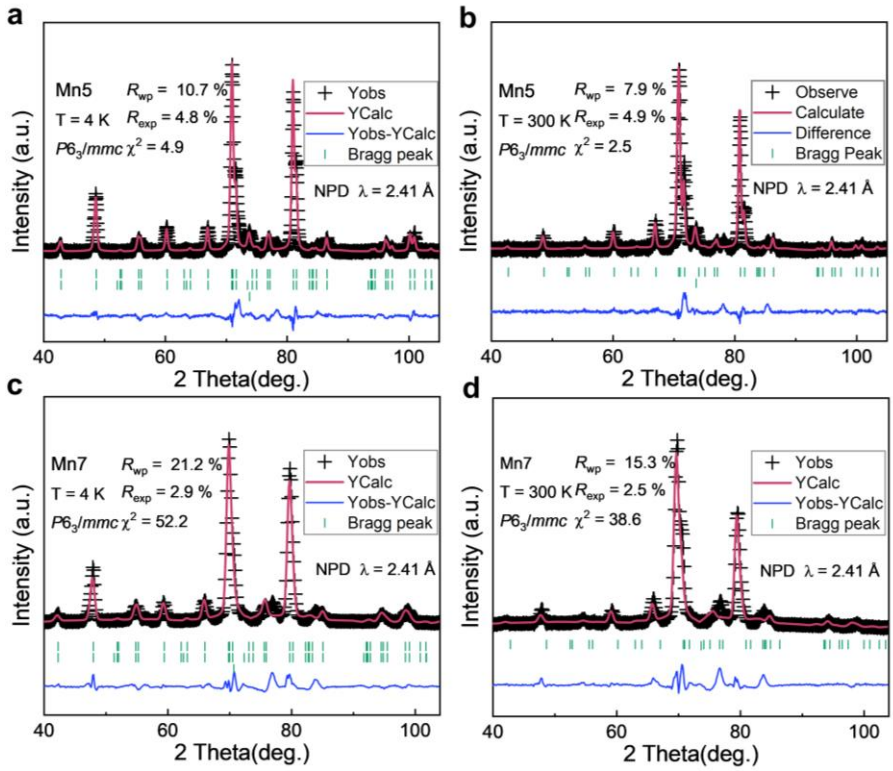

Figure S19. Rietveld refinements of neutron powder diffraction (NPD) pattern of **Mn5** (a) and **Mn7** (c) at 4 K (λ = 2.41 Å), **Mn5** (b) and **Mn7** (d) at 300 K. Rietveld refinement based on the FiM structure can well fit the patterns. The moment of Mn and Fe at the same position is restricted to better convergence.

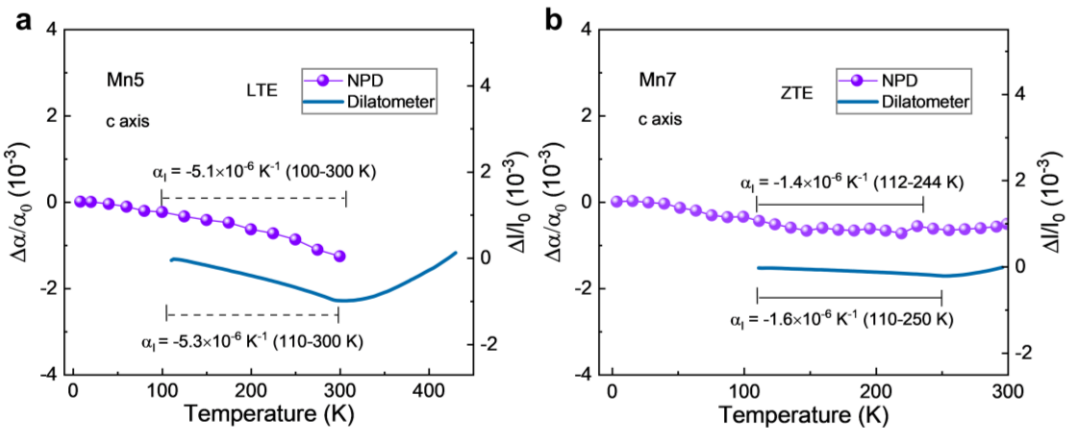

Figure S20. Negative thermal expansion along *c* axis of **Mn5** (a) and **Mn7** (b) measured by both dilatometer and NPD.

Table S3. The cell parameters and magnetic moments at each site of **Mn5** and **Mn7** compounds at 3 K/4 K were obtained by refinement.

Sample composition		Mn5	Mn7
Lattice Parameter at 3 K/4 K (A)	*a*,*b*	8.41297(4)	8.42239(32)
	c	8.33734(4)	8.34991(51)
	V	511.042(7)	512.959(42)
Magnetic moment at 3K/4 K (μB)	Ho (2b/2c/2d)	10.15(14)	9.95(22)
	Fe/Mn (4f/4e)	-0.55(5)	0.54(26)
	Fe/ Mn (6g)	-1.17(11)	-1.17(24)
	Fe/ Mn (12j)	-1.50(10)	-1.73(20)
	Fe/ Mn (12k)	-1.37(8)	-1.20(16)
	$\Sigma M_{Fe/Mn}$	21.8(15)	20.0(21)
	ΣM_{Ho}	20.3 (2)	19.9 (4)
	$\Sigma M_{Ho2(Fe,Mn)17}$	1.5(17)	0.1(25)

It can be found that the magnetic moments of the Fe/Mn-sublattice are almost equal to that of the Ho-sublattice at low temperature, thus a near zero net magnetic moment of **Mn5** and **Mn7**. The conventional FiM state is observed in the intermediate temperature because the moments of Ho decrease quickly and that of Fe/Mn-sublattice turn to dominate. The refined magnetic moment at the 12j site is 1.73 μ_B/atom much smaller than that of Ho_2Fe_{17} (~ 2.7 μ_B/atom), so the Mn should be AFM coupled with Fe-sublattice. By varying the content of Mn, the net-magnetic moment decreases and the fully cFiM is obtained on **Mn7** sample. We calculate the total moment between the adjacent atomic layers, the kagome layer is ferromagnetic, and the moment of Ho-layer is almost zero, indicating a compensated FiM. Such FM/FiM interface may provide unusual pinning effects in $Ho_2Fe_{17}Mn_\delta$.

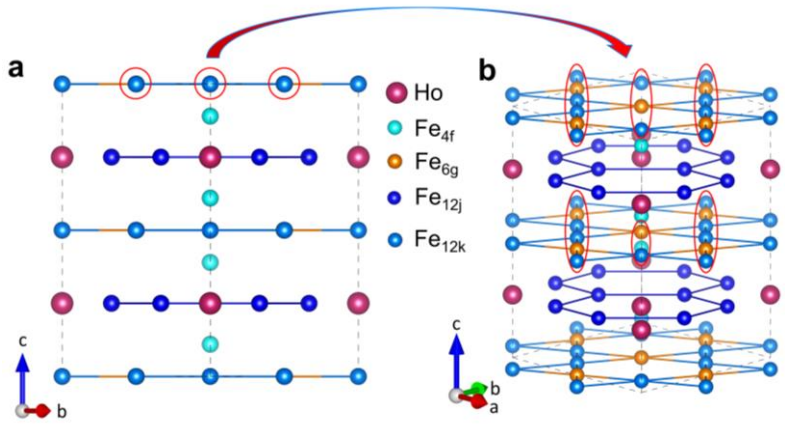

Figure S21. (a) Crystal structure of hexagonal phase along the [$\bar{1}$10] zone axis in **Ho_2Fe_{17}** compound, in which the Fe_{6g} and Fe_{12k} alternately stacked in the kagome layer in this direction (b), combined with EELS patterns, the blank Mn region of the kagome layer indicated that Mn occupies the Fe_{4f} sites rather than the Fe_{6g} or Fe_{12k} sites.

Table S4. Fitting results for ^{57}Fe Mössbauer spectrum of **Mn5** compound at 25 K.

		Isomer Shift (mm/s)	Quadrupole Splitting(mm/s)	Magnetic Hyperfine Field (T)
	4f	0.37 (6)	-0.30 (11)	29.0(3)
	$6g_1$	0.24(3)	-0.24(7)	25.3(2)
	$6g_2$	-0.001(30)	0.21(6)	22.4((3)
25 K	$12j_1$	-0.024(28)	0.12(6)	19.1(3)
	$12j_2$	-0.13(4)	0.03(6)	15.0(4)
	$12k_1$	0.15(6)	-0.38(11)	16.7(6)
	$12k_2$	0.06(4)	-0.04(7)	4.0(3)

Table S5. Fitting results for ^{57}Fe Mössbauer spectrum of **Mn5** compound at 100 K.

		Isomer Shift (mm/s)	Quadrupole Splitting(mm/s)	Magnetic Hyperfine Field (T)
	4f	0.35(7)	-0.32 (13)	26.0(4)
	$6g_1$	0.26(7)	-0.25(13)	23.0(5)
	$6g_2$	-0.001(42)	0.17(7)	20.6((4)
100 K	$12j_1$	0.03(3)	0.09(7)	17.4(4)
	$12j_2$	-0.10(4)	0.09(6)	13.6(3)
	$12k_1$	0.13(4)	-0.39(7)	15.1(3)
	$12k_2$	0.04(3)	0.03(5)	3.9(2)

Table S6. Calculated atomic moments, and total magnetization per f.u. (in $\mu_{B)}$ for ferrimagnetic states (Ferri) with all Mn moments oriented antiparallel to Fe moments, and ferrimagnetic states where Mn moments form random antiferromagnetic structure on 12j sub-lattice (RAFM). For RAFM structure the Mn moments are given for two sub-lattices with parallel and antiparallel orientation to ferromagnetic Fe moment matrix. The calculated total energies of Ferri and RAFM structures are degenerated within computational accuracy (better than 0.1 meV/atom) for **Mn5** alloy. For **Mn7** alloy the Mn-RAFM structure has lower energy than purely ferromagnetic one by 0.2 mRy/atom. (Ho sites have additional localized 4f-moment = 10 mb, oriented in negative direction).

Ho	Ho_2Fe_{17}	Mn5 (Ferri)	Mn5 (Mn-RAFM)	Mn7 (Ferri)	Mn7 (Mn-RAFM)
m(Fe), 12k	2.30	1.97	1.94	1,93	1.89
m(Fe), 12j	2.41	2.24	2.20	2.24	2.18
m(Mn), 12j	-	-1.96	1.38 (-2.27)	-1.79	1.49(-2.16)
m(Fe), 6g	1.97	1.67	1.62	1.62	1.57
m(Fe), 4f	2.66	2.23	2.27	2.24	2.26
m(Mn), 4f	-	-1.89	-1.98	-1.94	-1.97
m(Ho), 2d	-10.50	-10.38	-10.41	-10.35	-10.38
m(Ho), 2b	-10.56	-10.39	-10.42	-10.35	-10.38
M(total) per f.u.	18.47	-2.41	1.88	-6.50	-1.68

Table S7. Calculated inter-atomic magnetic exchange interactions (Hamiltonian 1) in **Mn5** alloy between different atoms on different sub-lattices (in mRy) in **Mn5** alloy. Only interactions larger than 0.05 mRy are shown. Positive sign is FM_interactions, negative is AFM. Due to very strong AFM interaction between Mn sites in 12j sublattice, Mn forms random AFM structure on 12j sublattice (in both **Mn5** and **Mn7** alloys). There is also extremely strong AFM interaction between Mn, 4f and Mn, 4f means that Mn4f "gantel" (when two Mn meet on the edges of the gantel) form strong AFM dimer. Despite that our 2:17 structure is more complicated than that simple Heusler alloy, where there is only a single magnetic Fe/Mn sub-lattice of fcc type there is a strong similarity. Our neutron diffraction analyses have suggested that Mn in 2:17 occupies only 12j and 4f position. The **Mn5** composition with large coercivity corresponds to the case where 12j and 4f positions are almost equally occupied by Fe and Mn atoms, whereas Mn7 alloy, with vanishing coercivity, is the composition where 12j and 4k positions become reach in Mn. Thus, we observed essentially a similar phenomenon like in corresponding Heusler compounds accompanied by the appearance of the large exchange bias in the compositions with large coercivity.[19,20] To further understand the instability of pure ferromagnetic state with respect the RAFM state we calculate the inter-atomic exchange interactions for the following Heisenberg Hamiltonian:

$$H = -\sum_{\substack{i,j\in 12k,12j \\ 6g,4f}} J_{ij}^{Fe-Fe}\vec{e}_i^{Fe}\,\vec{e}_j^{Fe} - \sum_{\substack{i\in 12k,12j,6g,4f \\ j\in 12j,4f}} J_{ij}^{Fe-Mn}\vec{e}_i^{Fe}\,\vec{e}_j^{Mn} - \sum_{\substack{i\in 12k,12j,6g,4f \\ j\in 2b,2d}} J_{ij}^{Fe-Ho}\vec{e}_i^{Fe}\,\vec{e}_j^{Ho}$$
$$- \sum_{i,j\in 12j,4f} J_{ij}^{Mn-Mn}\vec{e}_i^{Mn}\,\vec{e}_j^{Mn} - \sum_{\substack{i\in 12j,4f \\ j\in 2b,2d}} J_{ij}^{Mn-Ho}\vec{e}_i^{Fe}\,\vec{e}_j^{Ho} - \sum_{i,j\in 2b,2d} J_{ij}^{Ho-Ho}\vec{e}_i^{Ho}\,\vec{e}_j^{Ho}$$

Where $\vec{e}_i^{A}$ are the unit vectors of the spin moment directions on the corresponding lattice sites of A-atomic component. To this end we use the Green function based magnetic force theorem[21] implemented in the KKR method[22] and applied it in combination with CPA allowing for the effects of the atomic disorder on 4f and 12j sub-lattices.

References.

1. Perdew, J. P.; Wang, Y. Accurate and simple analytic representation of the electron-gas correlation energy. *Phys. Rev. B.* **1992,** 45, 13244-13249.

2. Ruban, A.; Skriver, H. L. Calculated surface segregation in transition metal alloys. *Comp. Mater. Sci.* **1999,** 15, 119-143.

3. Khmelevskyi, S.; Khmelevska, T.; Ruban, A. V.; Mohn, P. Magnetic exchange interactions in the paramagnetic state of hcp Gd. *J. Phys-Condens. Mat.* **2007,** 19, 326218.

4. Moreno, R.; Khmelevskyi, S.; Chubykalo-Fesenko, O. Role of exchange parameters for ultrafast thermally induced magnetization switching in ferrimagnets. *Phys. Rev. B.* **2019,** 99, 184401.

5. Moreno-Pineda, E.; Taran, G.; Wernsdorfer, W.; Ruben, M. Quantum tunnelling of the magnetisation in single-molecule magnet isotopologue dimers. *Chem. Sci.* **2019,** 10, 5138-5145.

6. Lin, S.; Shao, D. F.; Lin, J. C.; Zu, L.; Kan, X. C.; Wang, B. S.; Huang, Y. N.; Song, W. H.; Lu, W. J.; Tong, P.; Sun, Y. P. Spin-glass behavior and zero-field-cooled exchange bias in a Cr-based antiperovskite compound $PdNCr_3$. *J. Mater. Chem. C.* **2015**, 3, 5683-5696.

7. Li, M. M.; Shen, J. L.; Wang, X.; Ma, L.; Li, G. K.; Zhen, C. M.; Hou, D. L.; Wang, M. Enhanced antiferromagnetic interaction-induced spontaneous exchange bias in $Mn_{50}Ni_{40}Sn_{10-x}Ti_x$ Heusler alloys. *Intermetallics* **2018**, 96, 13-17.

8. Lin, J. C.; Tong, P.; Cui, D. P.; Yang, C.; Lin, S.; Lu, W. J.; Wang, B. S.; Zhao, B. C.; Sun, Y. P. Exchange bias induced after zero-field cooling in antiperovskite compounds $Ga_{1-x}NMn_{3+x}$. *Phys. Status. Solidi. B.* **2015**, 252, 582-588.

9. Han, Z. D.; Qian, B.; Wang, D. H.; Zhang, P.; Jiang, X. F.; Zhang, C. L.; Du, Y. W. Magnetic phase separation and exchange bias in off-stoichiometric Ni-Mn-Ga alloys. *Appl. Phys. Lett.* **2013**, 103, 172403.

10. Anuraag, N. S.; Shaw, S. K.; Meena, S. S.; Singh, R. K.; Prasad, N. K. Spontaneous exchange bias in high energy ball milled MnBi alloys. *J. Magn. Magn. Mater.* **2022,** 557, 169478.

11. Wang, B. M.; Liu, Y.; Ren, P.; Xia, B.; Ruan, K. B.; Yi, J. B.; Ding, J.; Li, X. G.; Wang, L. Large exchange bias after zero-field cooling from an unmagnetized state. *Phys. Rev. Lett.*

2011, 106, 077203.

12. Jia, L.; Shen, J.; Li, M.; Wang, X.; Ma, L.; Zhen, C.; Hou, D.; Liu, E.; Wang, W.; Wu, G. Tuning antiferromagnetic exchange interaction for spontaneous exchange bias in MnNiSnSi system. *APL. Materials.* **2017**, 5, 126105.
13. Nayak, A. K.; Nicklas, M.; Chadov, S.; Shekhar, C.; Skourski, Y.; Winterlik, J.; Felser, C. Large zero-field cooled exchange-bias in bulk Mn_2PtGa. *Phys. Rev. Lett.* **2013,** 110, 127204.
14. Liao, X.; Wang, Y.; Wetterskog, E.; Cheng, F.; Hao, C.; Khan, M. T.; Zheng, Y.-Z.; Yang, S. Superposition of conventional and spontaneous exchange bias in a $Ni_{50}Mn_{34}In_{13}Fe_3$ magnetic shape memory alloy. *J. Alloys. Compd.* **2019**, 772, 988-993.
15. Wang, B. M.; Liu, Y.; Xia, B.; Ren, P.; Wang, L. Large exchange bias obtainable through zero-field cooling from an unmagnetized state in Ni-Mn-Sn alloys. *J. Appl. Phys.* **2012**, 111, 043912.
16. Ding, L.; Chu, L.; Manuel, P.; Orlandi, F.; Li, M.; Guo, Y.; Liu, Z. Giant spontaneous exchange bias in an antiperovskite structure driven by a canted triangular magnetic structure. *Materials Horizons* **2019**, 6, 318-325.
17. Tian, F.; Cao, K.; Zhang, Y.; Zeng, Y.; Zhang, R.; Chang, T.; Zhou, C.; Xu, M.; Song, X.; Yang, S. Giant spontaneous exchange bias triggered by crossover of superspin glass in Sb-doped $Ni_{50}Mn_{38}Ga_{12}$ Heusler alloys. *Sci. Rep.* **2016**, 6, 30801.
18. Liao, P.; Jing, C.; Wang, X. L.; Yang, Y. J.; Zheng, D.; Li, Z.; Kang, B. J.; Deng, D. M.; Cao, S. X.; Zhang, J. C.; Lu, B. Strongly enhanced antiferromagnetism and giant spontaneous exchange bias in $Ni_{50}Mn_{36}Co_4Sn_{10}$ Heusler alloy. *Appl. Phys. Lett.* **2014**, 104, 092410.
19. Mizusaki, S.; Douzono, A.; Ohnishi, T.; Ozawa, T. C.; Samata, H.; Noro, Y.; Nagata, Y. Effect of Fe substitution on magnetic properties of antiferromagnetic Heusler alloy Ru2MnGe. *J. Alloys. Compd.* **2012,** 510, 141-146.
20. Douglas, J. E.; Levin, E. E.; Pollock, T. M.; Castillo, J. C.; Adler, P.; Felser, C.; Krämer, S.; Page, K. L.; Seshadri, R. Magnetic hardening and antiferromagnetic/ferromagnetic phase coexistence in $Mn_{1-x}Fe_xRu_2Sn$ Heusler solid solutions. *Phys. Rev. B.* **2016,** 94, 094412.
21. Liechtenstein, A. I.; Katsnelson, M.; Antropov, V.; Gubanov, V. Local spin density

functional approach to the theory of exchange interactions in ferromagnetic metals and alloys. J. Magn. Magn. Mater. **1987,** 67, 65-74.

22. Ruban, A. V.; Simak, S. I.; Shallcross, S.; Skriver, H. L. Local lattice relaxations in random metallic alloys: Effective tetrahedron model and supercell approach. *Phys. Rev. B.* **2003,** 67, 214302.